Original Article

Temperature dependent broadband dielectric, magnetic and electrical studies on $Li_{1-x}Mg_{2x}Fe_{5-x}O_8$ for microwave devices

Prajna P. Mohapatra [a], Suresh Pittala [b], Pamu Dobbidi [a],*

[a] *Department of Physics, Indian Institute of Technology Guwahati, Guwahati 781039, India*
[b] *Department of Physics, Indian Institute of Science, Bangalore, Karnataka 560012, India*

ABSTRACT

Polycrystalline samples of Mg substituted lithium ferrites ($Li_{1-x}Mg_{2x}Fe_{5-x}O_8$ (LMFO) ($x = 0$, 0.003, 0.005, 0.007 and 0.01) have been prepared by conventional solid-state reaction. X-ray diffraction patterns revealed the formation of a single-phase cubic structure with $P4_132$ space group. The dielectric constant of lithium ferrite increased with Mg substitution attaining a maximum value for $x = 0.005$ ($\varepsilon_r = 3034$, $tan\ \delta = 0.001$ at 1 MHz) at room temperature. Temperature-dependent dielectric response in the high frequency range (1 MHz–1 GHz) showed the relaxor behaviour of the dipoles, evident from the shift in the loss tangent with frequency. The activation energy of LMFO is found to be in the range of 1.39 - 0.35 eV. An enhanced permeability is found to be $\sim$29 for $x = 0.007$ at 1 MHz, RT. The variation in permeability is attributed to the variation in thickness of the domain walls and magneto-crystalline anisotropy. The temperature-dependent magnetization curves reveal the ferrimagnetic transition of LFO at 600 °C, which reduced with Mg substitution. Magnetic hysteresis loops showed the highest saturation magnetization (M_s = 54.6 emu/g) for $x = 0.007$ among all the samples. The magnetic properties are explained by considering Neel's two sub-lattice model. Thus, LMFO samples, (especially with $x = 0.005$) are very promising for circulator and phase shifter applications.

1. Introduction

Spinel ferrites are materials that have attracted much attention for a long time by virtue of their unique optical, electric, and magnetic properties [1–3]. Therefore, these materials are very promising for various applications in novel technological devices such as circulator, gyrator, phase shifter, etc. [4,5].

Among the spinel ferrites, lithium ferrite ($LiFe_5O_8/Li_{0.5}Fe_{2.5}O_4$) (LFO) has been extensively studied owing to its chemical stability, exceptional magneto-dielectric properties. LFO exhibits high Curie temperature (T_c), square hysteresis loop, high saturation magnetization (M_s), excellent dielectric properties, and high resistivity, etc. [6,7]. Because of its low cost, it can be a better substitution for extensively used yttrium iron garnet (YIG) for microwave applications [8,9]. Furthermore, they are also used in lithium-ion batteries, memory, and magnetic recording devices, magnetic resonance imaging

enhancement, magneto-caloric refrigeration, and gas sensing applications [10–16].

Lithium ferrite (soft ferrimagnetic material) exists in the form of bcc cubic crystal lattice having an inverse spinel structure (AB_2O_4), in which A and B occupy tetrahedral and octahedral sites, respectively. The 8A and 16B sites in cubic spinel ferrites are occupied by iron and divalent cations [17]. The effect of cationic ordering on the ferromagnetic resonance (FMR) and the structural properties of single-crystal LFO have been investigated by Pachauri [18]. Different preparation methods have been used to synthesize lithium ferrite (LFO), such as sol-gel [19], solvothermal [20], microemulsion [21], spray pyrolysis [22], coprecipitation [23], microwave-induced combustion [24], etc. Moreover, dielectric and magnetic properties of lithium ferrite can be tailored and optimized to device-specific by choosing appropriate chemical substitutions with nonmagnetic ions. Soibam et al. [25] reported that the replacement of Co^{2+} does not affect quadrupole splitting and isomer shift. It is reported that the aluminium (Al) substituted lithium ferrite nanoparticles prepared using citrate gel auto combustion method show a reduction in the saturation magnetization [26]. Whereas the substitution of Ca on Li-Zn ferrite is found to enhance porosity and degrades the permeability. Sattar et al. [27] found that the replacement of Ca in place of Zn is a better option for improving electrical and magnetic properties rather than for Fe and Li. Rathod [28] et al. explained the correlated vibrations of the octahedral and tetrahedral complexes and the absorption bands in FTIR spectra of Li-Zn ferrites. Hilli et al. [29] studied the electro-magnetic properties of samarium (Sm) doped LFO nanoparticles. The resistivity of Sm doped LFO increased with Sm concentration. Bamme et al. [30] reported the dielectric properties of Cd substituted LFO using the microwave-induced combustion method. The dielectric constant degraded with Cd substitution and the quality factor shows cusps in the frequency range of 80–400 kHz. The citrate precursor method was used to prepare nanosized zirconium (Zr), and manganese (Mn) substituted LFO [31]. With an increase of Zr and Mn content, DC electrical resistivity enhanced, which follows the polaron hopping mechanism.

Similarly, with the increase in Zr–Co concentration, coercivity increases, but saturation magnetization decreases [32]. Nutan et al. [4] studied the complex permittivity, and permeability of Co substituted LFO for microwave applications. Argentina et al. [33] reported that LFO is better than the magnesium ferrites and nickel ferrites used at the microwave frequency region due to its relative effectiveness. El-Shaarawy et al. [10] studied structural, dielectric behavior, and ac conductivity in the lower frequency range (20 Hz–10 MHz) of Mg-doped LFO powders and found that AC conductivity increased with Mg concentration. Due to the high Curie temperature, high electrical resistivity, and low production cost, magnesium substituted LFO has been used in many electrical devices for high-frequency applications [34]. Nevertheless, most of the studies with this material focused either purely on the magnetic properties or electrical and dielectric properties at lower frequency regions, whereas the ferrite grains were more effective in high frequency regime. However, to the best of our knowledge, there is no study available on the temperature-dependent broadband dielectric properties and permeability measurements, which are essential for figuring out the stability of the devices fabricated with these ceramics. Further, to use this material for microwave device applications, it is necessary to have an understanding of both ε_r, μ_r, and their loss tangents along with the magnetic properties.

Therefore, it is interesting to investigate the broadband frequency (1 MHz–1 GHz) and temperature-dependent dielectric response, and permeability of Mg-substituted lithium ferrites. In this study, the conventional solid-state reaction method is used to prepare the Mg-substituted spinel lithium ferrite. In the present study, the objective of substituting Mg is to lower the loss tangent, as lithium ferrite exhibit higher loss tangent, and the minimization of loss tangent is essential for microwave applications. The substitution of divalent ions (Mg^{2+}) in the place of monovalent (Li^+) and a trivalent cation (Fe^{3+}) also affects bond length (Fe—O, Li—O) and bond angle Fe—OF—e, which eventually asserts influence on the electric and magnetic properties. The effect of Mg-substitution on structural, microstructural, and magnetic response is studied; dielectric and permeability responses are investigated in broad frequency ranges at different temperatures (−140–250 °C). Further, the electrical conductivity of these samples is also studied.

2.   Experimental procedure

Polycrystalline $Li_{1-x}Mg_{2x}Fe_{5-x}O_8$; $x = 0$, 0.003, 0.005, 0.007 and 0.01 (LMFO) were prepared by the conventional solid-state reaction method using commercially available constituents. The starting reagents were Fe_2O_3 (purity 99%, M/s JiangXi-HaiTe Advance Material, China), MgO (purity 99%, M/s Sigma Aldrich) and Li_2CO_3 (purity 99%, M/s Sigma Aldrich) were used as in stoichiometric ratio. The starting materials were pulverized using a planetary ball mill (M/s Fritsch, Pulverisette 6), and the obtained powders were calcined at 800 °C for 3 h. The calcined powders were re-milled again for 5 h (to reduce particle size and enhance the density) and compacted into two different shapes disc (diameter – 10 mm, thickness – 1 mm) for electrical and toroidal shapes for permeability measurements. To obtain the maximum relative density, initially, the samples were sintered at different temperatures, and it was found that the sample sintered at 1050 °C exhibited the maximum relative density. Therefore, further studies were carried out with these samples. The Archimedes method was used to determine the relative density of the sintered samples.

The structural characterizations of the prepared samples were studied using X-ray diffractometer (M/s Rigaku TTRAX-III, 18 kW, Cu-K_α radiation $\lambda = 1.5405$ Å) in the 2θ range of 20° to 70°. Field emission scanning electron microscopy (FE-SEM) (M/s Zeiss, Sigma) was used to record the surface morphology. The temperature and frequency-dependent dielectric constant (ε_r), dielectric loss ($tan\ \delta$) and permeability (μ_r) were measured from −140 °C to 250 °C in the frequency range of 1 MHz to 1 GHz using impedance and material analyzer (M/s Agilent Technologies, 4991A) with a basic accuracy of ±0.8% attached to an automatic temperature controller (M/s Novocontrol, BDS 2300). The magnetic cell (M/s Agilent Tech-

nologies, 16454A) was used for measuring the permeability of the prepared samples. Vibrating Sample Magnetometry (VSM) (M/s Lakeshore, 7410 series) with field accuracy ±0.05% was used to carry out high-temperature magnetic measurements. Magnetization was also measured at low-temperature ranges (10 K – 300 K) by using the physical property measurement system (M/s Quantum Design, DynaCool) with noise levels less than 6E-7 emu.

3.   Result and discussion

3.1.   Structural analysis

The X-ray diffraction patterns (XRD) of LMFO ceramics sintered at 1050 °C are shown in Fig. 1(a). LFO is known to exist in two different crystalline phases: α-phase and β-phase. α-phase (ordered phase) exhibits FCC inverse spinel structure (space group - $P4_132$), while β-phase exhibits disordered phase (space group - Fd3−m). The observed XRD reveals the formation of cubic ferrite (JCPDS Card No. 82-1436), confirming that Mg-substituted LFO exists only in the α-phase. The presence of β-phase or any other secondary phases due to the substitution of Mg is not observed in XRD patterns, confirming the phase purity of the prepared samples. The enlarged view of the predominant diffraction peak (311) around $2\theta \sim 35°$ is depicted in Fig. 1(b). As the concentration of Mg increased, Bragg's reflections shifted towards lower angles, which resulted in an increase in the lattice parameters and cell volume (see Table 1) associated with the structural distortion due to dissimilar ionic radii of the Mg^{2+} (0.71 Å) with Li^+ (0.76 Å) and Fe^{3+} (0.64 Å).

Further analysis was carried out using the Rietveld refinement method to estimate the crystal phase, space group, and atomic positions by using FullProf Suite. Fig. 1(c) shows the representative refined XRD pattern for $x = 0.005$. It was noted that Mg substituted lithium ferrite was in a single-phase cubic structure with (space group - $P4_132$) [10]. The goodness of the fitting was estimated by the R-values, as listed in Table 1. To observe the cell distortion due to Mg substitution in LFO, the illustrative unit cells were produced by the Vesta software, as shown in Fig. 2. It is observed that the trigonal bipyramids of iron and lithium show a tilt as the Mg content increases. These tilts eventually affect the magnetic as well as electric properties, discussed in later part of this paper.

The lattice strain and crystallite size in the LMFO ceramics were estimated by using the Williamson-Hall plot method:

$$\beta \cos \theta = \frac{k\lambda}{D} + 4\varepsilon \sin \theta \qquad (1)$$

Where k is the shape factor, β the full-width half maxima (FWHM) of the diffraction peak, λ the incident X-ray wavelength, θ is the Bragg angle, D is the crystallite size, and ε is the strain [35]. Fig. 3 shows the plots between $\beta \cos\theta$ and $4 \sin\theta$. Strain and crystallite size was calculated from the fitted line listed in Table1. The crystallite size and strain were found to be in the range of 70–95 nm and 0.09%–0.15% for $x = 0$–0.01, respectively. The crystallite size and strain both were found to be enhanced with an increase in Mg content.

3.2.   Surface morphology analysis

The surface morphologies of the LMFO ceramics are shown in Fig. 4. It is observed that the pure and Mg-doped LFO samples exhibit uniform grain distribution with dense microstructure. The microstructure and grain size are strongly affected by Mg substitution. The density of the LMFO is found to increase with Mg concentration. The average grain size is measured by Image J software (linear intercept method), and the obtained grain sizes are in the range of 1.265–0.978 μm. The variations in the grain size can be explained by different parameters, such as the concentration of various ions and diffusion coefficient [36]. The grain size of the ferrites is highly influenced by the domain wall contributions in the low-frequency regime [37], which can also be seen in permeability. The flexibility of the grain boundary causes grain growth. Further, grain growth and re-crystallisations are related to the mobility of grain boundaries [36,38].

3.3.   Dielectric properties

3.3.1.   Dielectric dispersion with frequency
The frequency-dependent dielectric constant measured in the temperature range of −140 °C to 230 °C is shown in Fig. 5. The dielectric constant of the LMFO samples is found to decrease with applied frequency, which is a typical response of a linear dielectric. The contribution to the dielectric constant comes from different polarization mechanisms, such as ionic, electronic, interface, and dipole polarization, which influence the frequency-dependent dielectric response. In the high-frequency regime, the dielectric response mainly gets affected by a dipole, ionic, and electronic polarization; the frequency-dependent dielectric constant may also be explained based on the electron hopping mechanism and dipole relaxation. The reduction of dielectric constant till 100 MHz can be due to the relaxation of dipoles. On an application of the external electric field, the interchange of electrons in between Fe^{3+} ↔ Fe^{2+} builds up local displacement of charges that causes polarization. Polarization reduces with an enhancement in frequency. The hopping of electrons is signed up to a particular frequency, beyond which it gets relaxed. Hence, ε_r becomes constant [39–41]. Whereas, the larger value of dielectric constant at lower frequency regime may be ascribed to grain boundary defects and predominance of Fe^{2+} ions. A similar kind of response is reported by Iqbal [31] and Surzhikov [40]. It is noted that the dielectric constant of the samples enhanced with Mg substitution up to $x = 0.005$ compositions and reduced further with the addition of Mg. This can be attributed to the higher polarizability of Mg, uniform grain size, and maximum relative density.

Dielectric constant improves with temperature, as can be seen from Fig. 5. At higher temperatures, the dipoles align easily, leading to a higher dielectric response. The dielectric response is enhanced with Mg substitution. From the earlier studies, it is found that Li^+ ions reside only at tetrahedral sites, whereas Mg^{2+} prefers both octahedral and tetrahedral sites. Hence, it replaces the Fe^{3+} ions to B-site from A- site. Consequently, more Fe^{2+}-Fe^{3+} ion pairs get accumulated at B-site, thus increasing the hopping mechanism [10]. Interestingly, $x = 0.005$ samples exhibited the best dielectric response at the
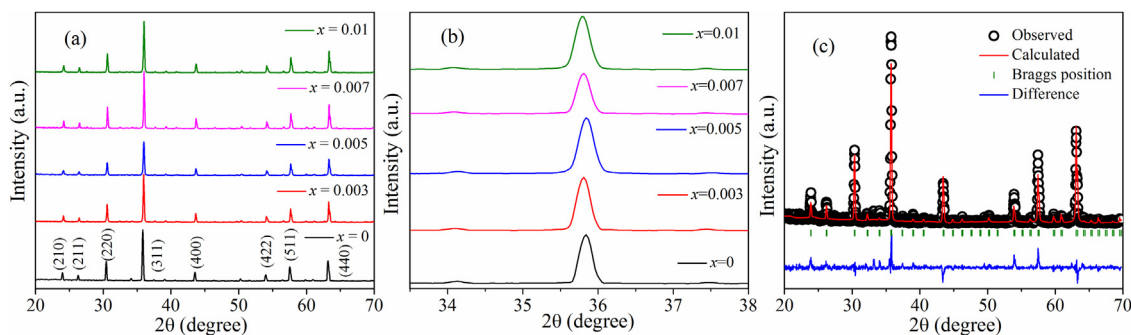
Fig. 1 – (a) X-ray diffraction pattern of $Li_{1-x}Mg_{2x}Fe_{5-x}O_8$ samples. (b) Zoomed portion of the XRD around 35°. (c) Refinement pattern of LMFO ($x = 0.005$).

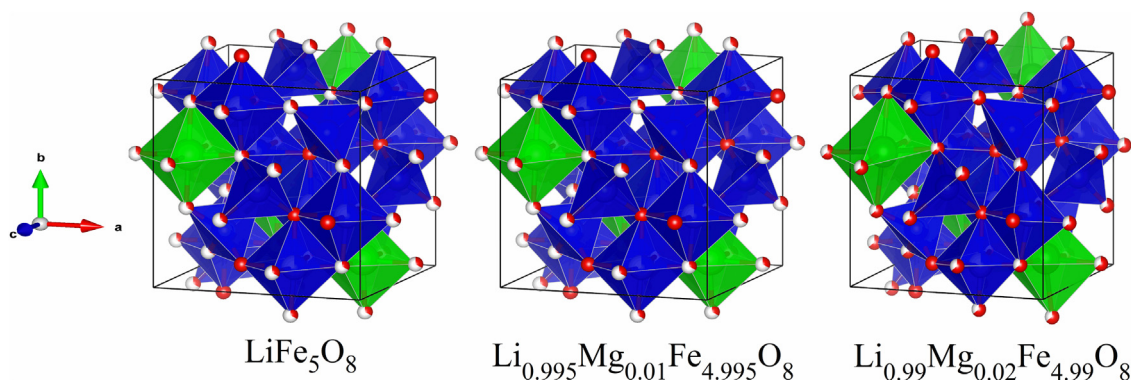| Table 1 – Unit cell parameters calculated from the XRD pattern of the LMFO ceramics.					
Composition	$x = 0$	$x = 0.003$	$x = 0.005$	$x = 0.007$	$x = 0.01$
$a = b = c$ (Å)	8.3259 (6)	8.3344 (4)	8.3293 (2)	8.3358 (4)	8.3506 (7)
V (Å³)	577.15	578.92	577.87	579.22	582.31
D (nm)	70.11	82.16	70.31	90.14	95.11
Strain	0.009	0.0011	0.0014	0.0014	0.0015
χ^2	1.76	2.89	2.53	2.92	2.62

Fig. 2 – Schematic representation of unit cells of LMFO. The green colour and the blue colour show the Li/Mg trigonal bipyramids and Fe/Mg trigonal bipyramids respectively.

whole measured temperature range, and all other samples displayed better dielectric response as compared to pure LFO. The values of dielectric loss and dielectric constant obtained at some frequencies and temperatures are listed in Table 2. Very low dielectric loss is achieved with Mg substitution when compared to previous reports [26,30,31].

3.3.2. Variation of the dielectric property with temperature

The temperature (-140 to 250 °C) dependent dielectric constant (ε_r) and dielectric loss ($tan\,\delta$) obtained at different frequencies are shown in Figs. 6 and 7, respectively. As the temperature increases from −140 °C, the dielectric constant of LFO initially increases and exhibits a hump at around 170 °C and then decreases for a further rise in temperature. This trend is also true for the other compositions; $x = 0.003$, 0.005, and 0.007. However, the hump in dielectric constant shifts toward higher temperatures with an increase in the Mg concentration, till $X = 0.007$. In contrast, for $x = 0.01$ samples, the dielectric constant increases continuously with temperature without

any hump or reduction in the values. The value of dielectric constant increases from 619 to 3034 while the dielectric loss reduces remarkably from 2.87 to 0.001 as the Mg concentration increases from $X = 0$ to $X = 0.005$ at RT. For LFO, as the temperature increases, $tan\,\delta$ rises initially exhibiting a cusp at −40 °C and again increases sharply above 170 °C at 1 MHz. The same trend is followed for all frequencies. The samples with $x = 0.003$, 0.005, and 0.007 also followed the same trend, but the hump shifts toward a lower temperature range. The shift in the hump is attributed to the relaxation of dipoles. For $x = 0.01$, the values of $tan\,\delta$ increase smoothly with temperature, accompanied by a sharp rise above 180 °C. The rise in dielectric response is attributed to the higher relative density, and the lattice distortion of the Mg substituted compounds. Further, it is found that the dielectric constant and dielectric loss are improved with an increase in temperature due to the displacements of localized charge carriers. However, the enhancement in the conductivity of the samples may be attributed to the increasing mobility of charge carriers as a result of applied
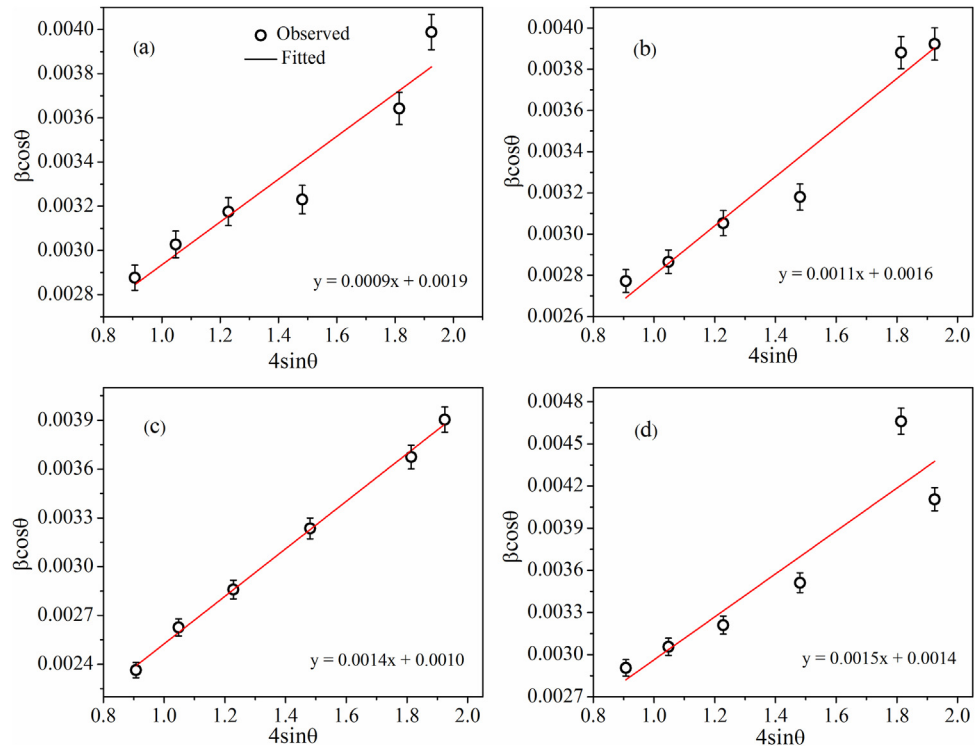
Fig. 3 – W-H plot of LMFO ceramics (a) $x = 0$, (b) $x = 0.003$, (c) $x = 0.005$, (d) $x = 0.01$.
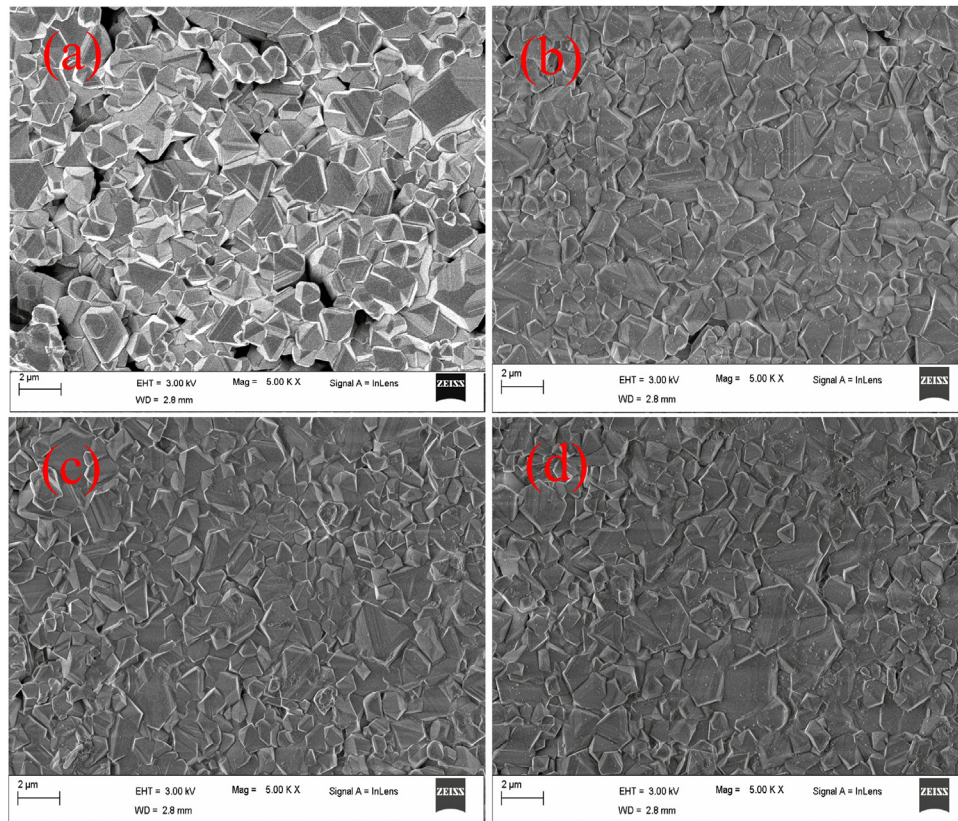

Fig. 4 – FE-SEM micrograph of the LMFO samples for (a) $x = 0$, (b) $x = 0.003$, (c) $x = 0.005$, (d) $x = 0.01$.
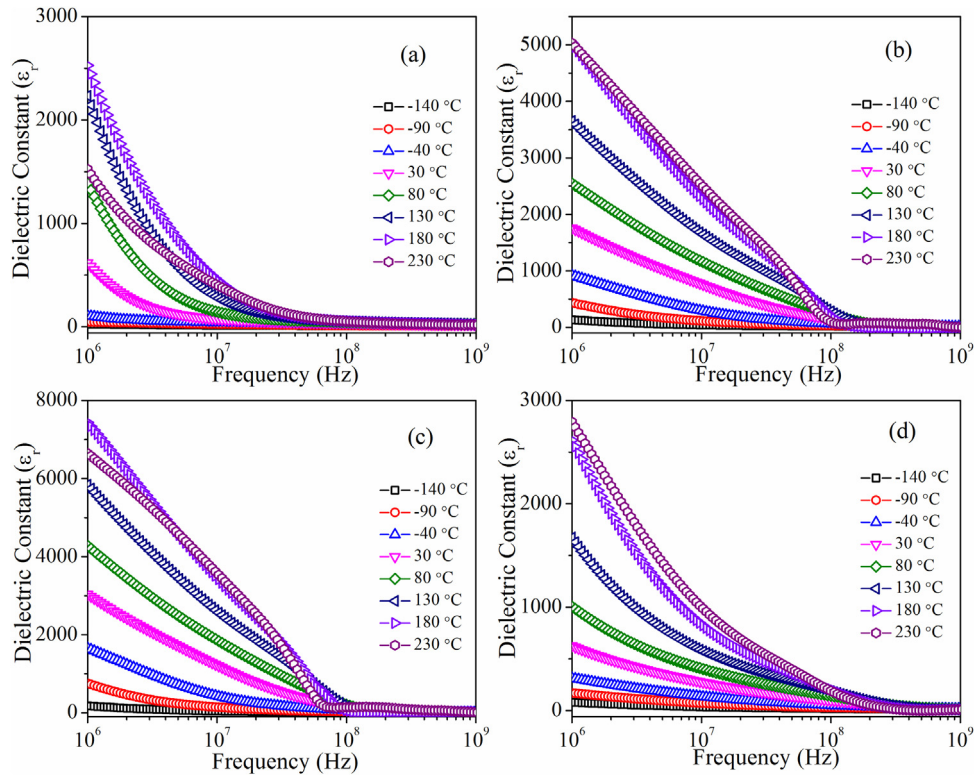
Fig. 5 – Frequency dependent dielectric constant of LMFO ceramics, measured at different temperatures (−140–230 °C) (a) $x = 0$, (b) $x = 0.003$, (c) $x = 0.005$, (d) $x = 0.01$.

Table 2 – The obtained permittivity and dielectric loss tangent values of LMFO ceramics.

Composition		$x = 0.00$		$x = 0.003$		$x = 0.005$		$x = 0.007$		$x = 0.01$	
Temp (°C)	Frequency	ε_r	Tanδ	ε_r	Tanδ (10^{-2})	ε_r	Tanδ (10^{-2})	ε_r	Tanδ (10^{-2})	ε_r	Tanδ (10^{-2})
−140	1 MHz	26	0.63	134	0.3	181	0.42	121	0.27	80	0.18
	10 MHz	13	0.40	40	0.29	45	0.31	36	0.28	35	0.16
	100MHz	10	0.14	20	0.12	21	0.15	20	0.10	20	0.11
	1 GHz	11	0.09	17	0.05	18	0.06	18	0.05	16	0.06
30	1 MHz	619	2.87	1759	0.15	3034	0.16	1670	0.16	626	0.20
	10 MHz	74	3.22	756	0.26	1201	0.28	723	0.23	273	0.26
	100MHz	36	0.91	139	0.56	143	0.88	157	0.51	96	0.31
	1 GHz	16	0.70	17	0.98	12	0.93	21	1.03	19	0.55
100	1 MHz	1733	3.51	2941	0.17	4859	0.16	3188	0.16	1226	0.26
	10 MHz	185	4.15	1333	0.22	2113	0.24	1350	0.23	463	0.25
	100MHz	48	1.81	239	0.66	174	1.03	250	0.67	155	0.36
	1 GHz	24	1.17	7.35	3.9	7	1.9	24	3.9	13	1.02
170	1 MHz	2614	4.64	4796	0.24	7227	0.23	5459	0.16	2449	0.32
	10 MHz	412	4.24	2135	0.23	3251	0.23	2306	0.24	765	0.33
	100MHz	53	4.00	211	1.12	61	1.4	205	1.6	192	0.53
	1 GHz	22	1.82	4	3.8	8	1.7	24	2.5	14	1.3
240	1 MHz	143	22.8	4857	1.85	6056	1.89	6738	0.90	2830	1.31
	10 MHz	315	9.75	2290	0.72	3129	0.71	3306	0.38	1060	0.60
	100MHz	37	8.39	121	1.62	66	1.5	29	2.1	128	1.2
	1 GHz	19	2.62	3	1.6	14	1.6	10	2.32	20	1.61

thermal energy. The observed high dielectric constant and low loss (order of 10^{-3}) in the high-frequency regime makes LMFO as a better candidate for microwave applications [33,42].

At lower temperatures, both the dielectric constant and loss tangents are lowered, and it is due to the lower thermal vibrations and the freezing of dipoles. Further, the substitution of
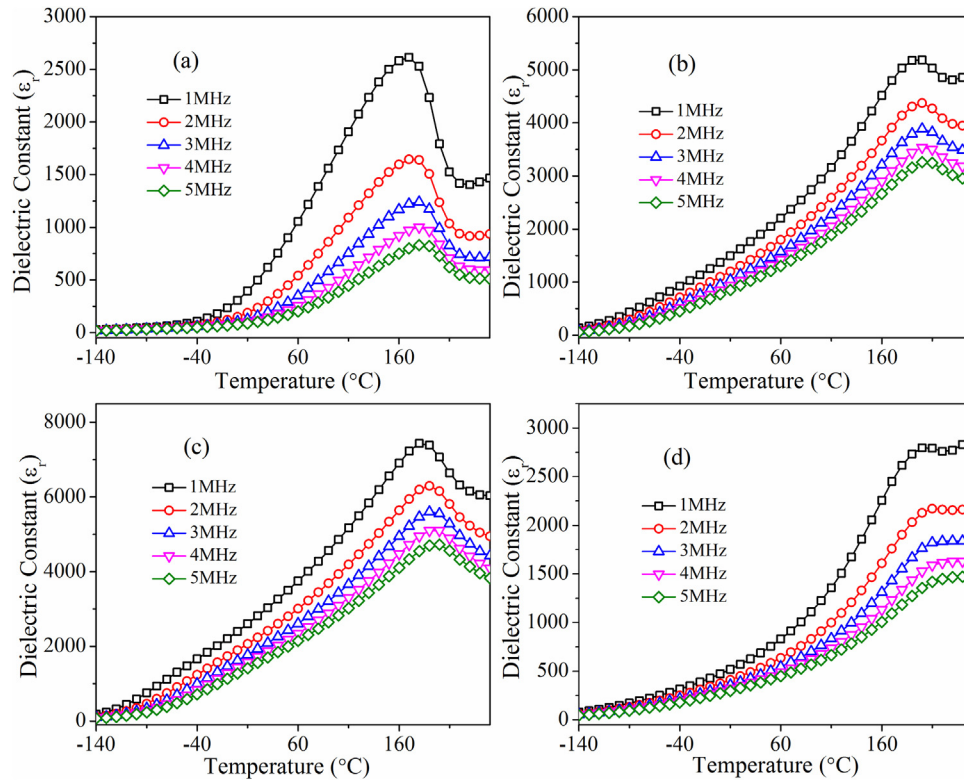
Fig. 6 – Temperature variation dielectric constant of LMFO ceramics, measured at different frequencies for (a) $x = 0$ (b) $x = 0.003$ (c) $x = 0.005$ (d) $x = 0.01$.
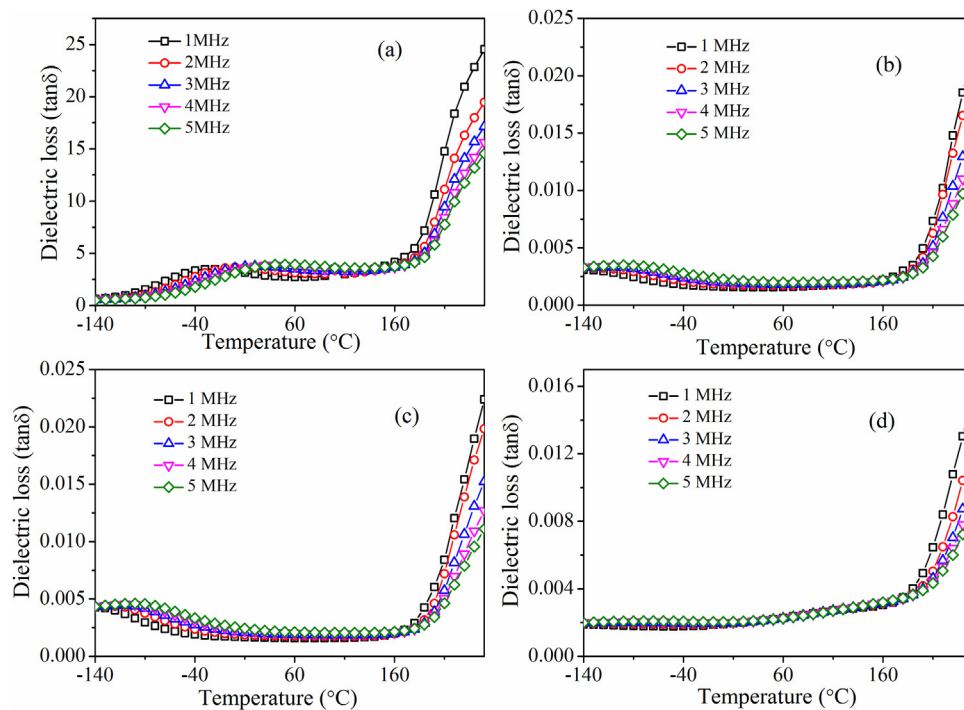

Fig. 7 – Temperature variation dielectric loss tangent of LMFO ceramics, measured at different frequencies for (a) $x = 0$ (b) $x = 0.003$ (c) $x = 0.005$ (d) $x = 0.01$.

Mg effectively minimized the loss tangent in these ceramics.

3.4. Electrical properties

By using the Arrhenius equation, activation energies (E_A) are extracted from temperature variation ac conductivity (σ_{ac}) [43].

$$\sigma_{ac} = \sigma_0 \exp(-E_A/k_B T) \qquad (2)$$

Where, σ_0, T, k_B is the pre-exponential factor, absolute temperature, and Boltzmann constant, respectively. The ln (σ_{ac}) vs 1000/T is plotted at 1 MHz for LMFO ($x = 0$, 0.003, 0.005, 0.007, 0.01), and is shown in Fig. 8(a). AC conductivity is found to increase with temperature and Mg^{2+} ion concentration. The principle of the electrical conduction mechanism can be understood by the dielectric polarization mechanism. The increase in the conductivity with a concomitant increase in temperature is because of thermally activated interchange of the charge carriers among Fe^{2+} and Fe^{3+}. Further, the increase in the conductivity due to Mg^{2+} ion is attributed to the concentration ratio of Fe^{3+}/Fe^{2+} ions on the B site. The activation energy is extracted from the slope of the fitted line and is found to be 1.39 eV for $x = 0$, which is decreased to 0.35 eV for $x = 0.005$. However, it shoots up again with an increase in Mg concentration.

The frequency variant ac conductivity can be explained by using the power equation.

$$\sigma_{ac}(w) = Aw^n \qquad (3)$$

where A is the temperature-dependent parameter, w the angular frequency, and n is dimensionless temperature-dependent parameter whose value lies between 0 and 1. For $n = 0$, the ac conductivity is independent of frequency, and for $n \leq 1$, the ac conductivity is dependent on frequency. Further, this region is divided into two parts, for $0.5 \leq n \leq 1$, the exchange of electron occurs among Fe^{2+} and Fe^{3+} ions, and for $n \leq 0.5$, the dominant contribution is from ionic conductivity. Fig. 8 (b) shows the logarithmic variation of room temperature σ_{ac} vs frequency. The ac conductivity increases with frequency, which is a typical characteristic of semiconducting materials. This behavior can also be explained using the pumping force corresponding to applied frequency, which is responsible for the hopping of charge carriers [26,44]. The value of n was calculated from the slope of the fitted curve. The obtained value for LFO is 0.138, which enhances with an increase in Mg concentration and the values are found in the range of 0.689 - 0.761, indicating the exchange of electrons between Fe^{2+} and Fe^{3+} ions.

3.5. Magnetic properties

Fig. 9 shows the variation of magnetization curves as a function of temperature (M-T) for LMFO samples. Magnetization decreases with an increase in temperature, which can be due to the fact that the iron spins at octahedral and tetrahedral sites are sealed in the direction of the applied magnetic field at low temperatures. With a rise in temperature, spins get

randomize due to thermal energy, resulting in the decrease of magnetization. Above a certain temperature, the magnetization becomes zero, which indicates a paramagnetic state. According to Fig. 9, the Curie temperature (T_c) of LMFO is shifted to lower temperatures as Mg concentration changes. The T_c for the pure LFO is 600 °C, and it decreases with Mg substitution; the values of T_c are listed in Table 3. The substitution of non-magnetic Mg^{2+} ions in place of iron ions in both A and B sites of AB_2O_4 lithium ferrite inverse spinel causes the A-B interaction to be weak, which leads to a reduction in magnetization, and the Curie temperature.

The room temperature M-H loop of LMFO ceramics are shown in Fig. 10(a). The values of coercivity (H_C), saturation magnetization (M_S), and remanent magnetization (M_r) are listed in Table 3 and plotted with Mg concentration in Fig. 10 (b). It is observed that saturation magnetization reduces as a function of Mg concentration. Nevertheless, the sample with $x = 0.007$ exhibits the highest saturation magnetization among all the other substituted samples. The observed magnetization could be due to the impact of several factors such as A-B exchange interaction, cation distribution, anisotropy, density, and grain size [26,45–48]. This can be better understood by Neel's two-sublattice model. According to Neel, three types of interactions exist A-A, B-B, and A-B. Among these, the superexchange A-B interaction is the strongest one. The resultant magnetization arises as a result of a vector sum of two sublattices A and B [49]. In order to accommodate the Mg^{2+} ions at the A-site, Fe^{3+} ions get transferred from A site to B site, which causes the initial decrease in saturation magnetization (M_s). Hence, Fe^{3+} ion content increases at B-site, causing the antiparallel spin coupling, which eventually results in the reduction of A-B exchange interaction strength, and consequently, decreases the magnetization. The increase in M_s for $x = 0.007$ may be due to Mg^{2+} ions, which are substituted for Li^+ and occupy the tetrahedral A site with an analogous transfer of Fe^{3+} from A to B site. This enhances the magnetization in the B site. The random behavior of H_C is attributed to the variation of particle size and magnetic anisotropy [50,51]. The Mg substitution on LFO leads to the structural distortion, as depicted in Fig. 3, which modifies Fe−OF−e bond angles at both the tetrahedral and octahedral positions and the Fe−O bond length (Table 3). Further, the magnetocrystalline anisotropy was determined by analyzing the initial M-H curve with the law of approach (LAP) to saturation [52]:

$$M = M_s \left[1 - \frac{8}{105\mu_0^2 M_s^2} \left(\frac{K_1}{H} \right)^2 \right] + \gamma H \qquad (4)$$

Where the coefficient 8/105 is the polycrystalline specimen with cubic anisotropy, K_1, and γH are the cubic anisotropy constant and forced magnetization due to the increase of saturation magnetization, respectively. Fig. 10 (c) shows the fitted curve of LAP with the experimental initial magnetization data. The anisotropy constant is found to decrease with Mg content, except for $x = 0.003$. The obtained values are 1.17E5 and 1.03E5 erg/cm³ for $x = 0.00$ and 0.007, respectively.

Fig. 11(a and b) shows the variation of zero-field cooled (ZFC) and field cooled (FC) magnetization as a function of temperature (10 K–300 K) for $x = 0$ and 0.007 samples. The ZFC curve is obtained by cooling the sample in zero field from room tem-
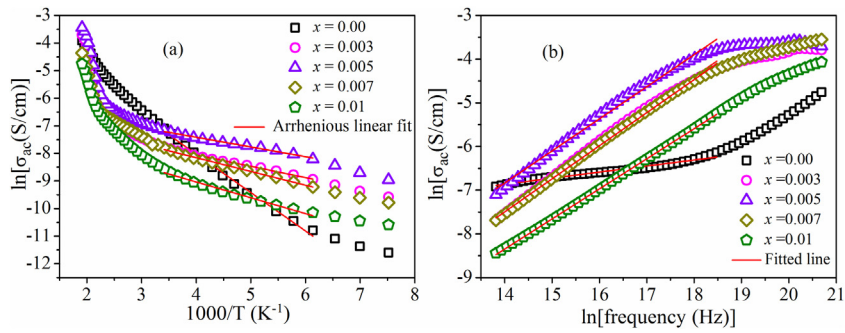
Fig. 8 – Logarithmic variation of σ_{ac} as a function of (a) 1000/T and (b) ln (frequency) of LMFO ceramics $x = 0$, 0.003, 0.005, 0.007 and 0.01.
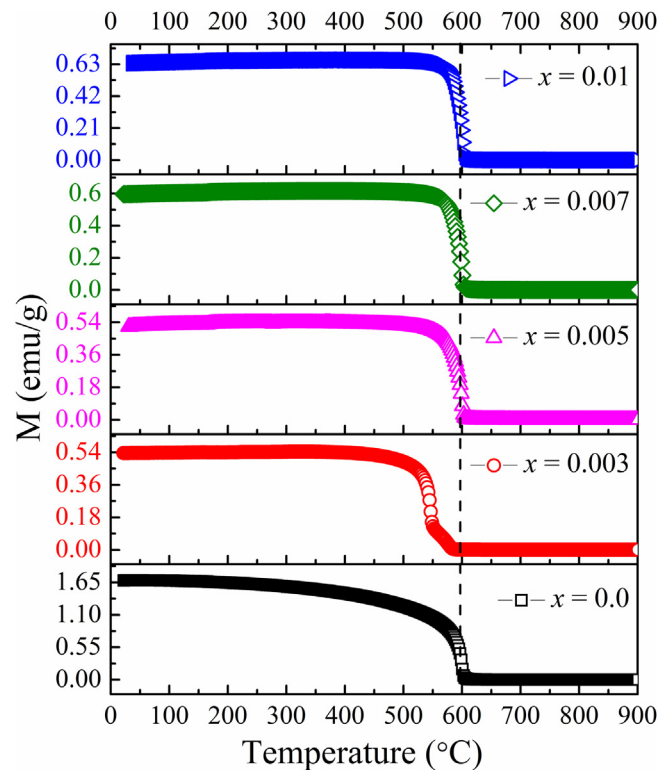

Fig. 9 – Temperature dependent magnetization curve of LMFO samples.

Table 3 – Magnetic parameters of LMFO ceramics.

Parameters	$x = 0$	$x = 0.003$	$x = 0.005$	$x = 0.007$	$x = 0.01$
M_s (emu/g)	59	48	50	55	53
M_r (emu/g)	5.44	3.51	3.32	3.75	4.78
H_c (Oe)	80.38	88.09	81.25	86.47	105.92
T_c (°C)	600	556	598	605	596
Fe—O (Å)	1.9236	1.9199	1.9188	1.9202	1.9237
Fe—OF—e (°)	121.20	120.15	123.48	127.56	132.39

perature to 10 K, then the magnetic field is applied at 10 K, and simultaneously magnetization is recorded while increasing the temperature. Similarly, FC magnetization is obtained by cooling the samples at 1 kOe. For LFO, ZFC and FC curves show a decrease in magnetization with an increase in temperature, and both curves merged at 203 K. However, for $x = 0.007$, ZFC curve initially increases with an increase in temperature

up to 30 K, then decreases, and merged with FC curve at 210 K. Similar kind of response is also observed by Shirsath [53] and Dar [54]. The slow relaxation of the particles and the existence of the energy barrier of magnetic anisotropy may be the main cause for bifurcation of ZFC and FC curve [21,55]. These particles have a low anisotropy energy barrier to overcome their energy barrier by the thermal activation energy. The *M-*
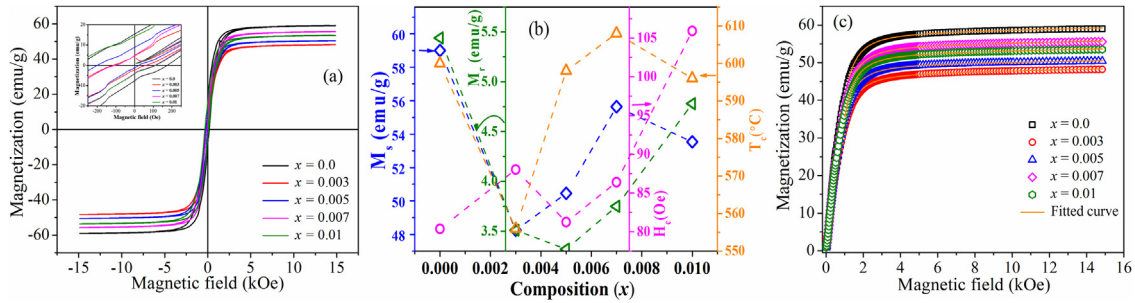
Fig. 10 – (a) Room temperature M-H curves of the LMFO. Inset shows the enlarged view near the origin. (b) The variation of magnetic parameters with Mg composition.
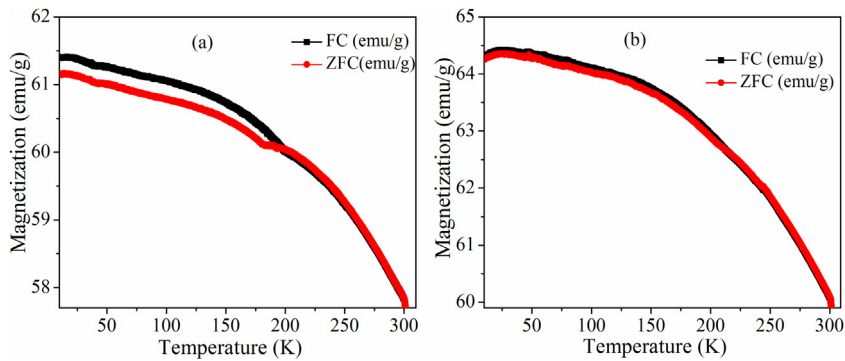

Fig. 11 – M-T curves below room temperature (10 K – 300 K) for (a) LFO and (b) x = 0.007.
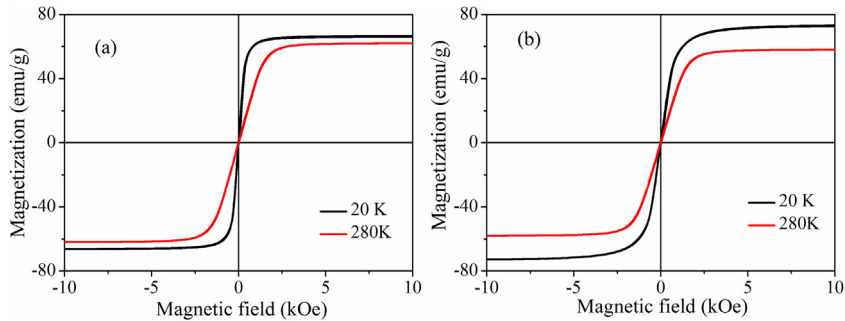

Fig. 12 – M-H loops below room temperature (20 K and 280 K) for (a) LFO and (b) x = 0.007.

H loop at 20 K and 280 K were recorded for x = 0.00 and 0.007, as shown in Fig. 12(a and b), respectively. The obtained saturation magnetization for LFO is 66.52 and 62.07 emu/g at 20 K and 280 K, respectively. The x = 0.007 exhibits enhanced saturation magnetization, 73.04 and 57.85 emu/g at 20 K and 280 K, respectively. The coercivity and remanent magnetization is improved with a decrease in temperature.

3.6. Permeability analysis

The frequency (1 MHz to 1 GHz) and temperature (-140 to 250 °C) dependent real part of permeability is plotted for LMFO ceramics, as shown in Fig. 13(a) and (b). The obtained permeability for pure LFO is $\mu_r = 27.88$ at 1 MHz frequency, which is a comparable value with previously reported data [56]. Permeability strongly influenced by Mg concentration. For x = 0.003, the permeability decreases to 23.94. However, for x = 0.005 and x = 0.007, the permeability raises to 28.56 and 29, accordingly.

The variation in permeability mainly depends on the thickness of the domain walls (δ), magneto-crystalline anisotropy (K_1), the average grain size (D_m), and inner stress (σ), which can be well understood by this relation [57].

$$\mu \propto \mu_0 M_S^2 D_m / \left[\kappa_1 + (3/2)\,\lambda_S \sigma \right] \beta^{1/3} \delta \tag{5}$$

where, M_s, λ_s, and β are the saturation magnetization, saturation magnetostriction constant, and volume concentration of impurity, correspondingly. According to the previous analysis (initial magnetization curve with Law of approach to saturation), K_1 decreased with Mg concentration, which can be ascribed to the enhanced permeability. A transition in the range of 70 to 90 °C is observed from the temperature-dependent permeability for all the LMFO ceramics. Fig. 13(c) shows the variation of magnetic loss as a function of frequency for LMFO ceramics. For LFO, the magnetic loss initially decreases with a rise in frequency up to 10 MHz and then
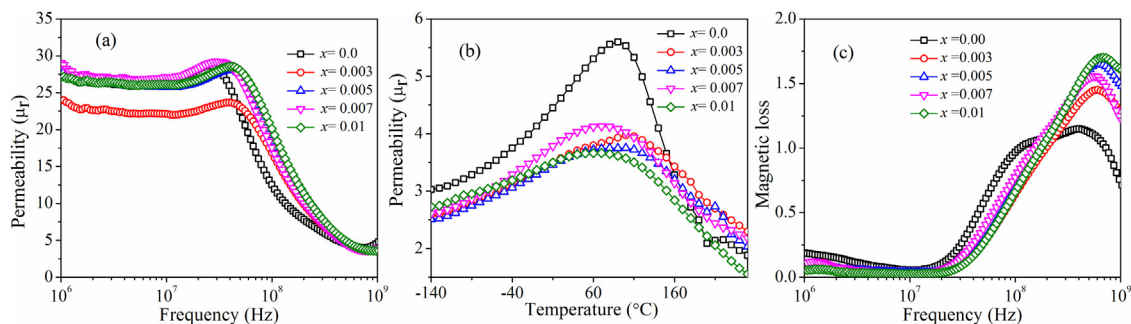
Fig. 13 – (a) Frequency variant permeability for LMFO ceramics measured at 30 °C, (b) Temperature variant permeability for LMFO ceramics at 1 GHz and (c) Frequency dependent magnetic loss for LMFO ceramics at RT.

increases exhibiting a broad peak at around 100 MHz. All other ceramics follow the same trend whereas, they exhibited a sharp peak with a shift towards higher frequency with Mg concentration.

According to the surface morphology analysis, Mg substituted LFO exhibited smaller grain size, which is ascribed to inhibition of grain growth due to Mg. From the dielectric response, it is found that with Mg substitution, the dielectric constant enhanced along with reduced loss tangent. This variation is explained based on the electron hopping mechanism. Again, magnetization decreased with an increase in Mg concentration, which is due to the change in cationic distribution and exchange interaction. Further, permeability response is correlated with magnetic and surface morphology results.

4. Conclusions

LMFO ceramics have been successfully synthesized by the conventional solid-state reaction method. XRD analysis and Rietveld refinement revealed the formation of a pure phase cubic spinel structure. All the ceramics exhibit dense microstructure. Enhanced dielectric (ε_r = 3034, $tan\ \delta$ = 0.001 at RT, 1 MHz) is observed for the Mg composition, x = 0.005. AC conductivity increases with an increase in temperature as well as Mg^{2+} concentration due to the exchange of electrons among Fe^{2+} and Fe^{3+} ions. The LMFO with x = 0.007 exhibits best permeability (μ_r = 29) and magnetic properties (M_s = 55.64 emu/g) at room temperature. The change in magnetic behaviour is explained by superexchange interactions and Neel's two sublattice models. A combination of high dielectric constant, low loss tangent (order of 10^{-3}), high permeability, and magnetic properties of LMFO make x = 0.005 specimens a good candidate for microwave applications such as phase shifter and the circulator.

Conflict of interest

In this paper, all the authors declare that there is no conflict of interest.

REFERENCES

[1] Joshi S, Kumar M, Chhoker S, Srivastava G, Jewariya M, Singh VN. Structural, magnetic, dielectric and optical properties of nickel ferrite nanoparticles synthesized by co-precipitation method. J Mol Struct 2014;1076:55–62, http://dx.doi.org/10.1016/j.molstruc.2014.07.048.

[2] Singhal S, Jauhar S, Singh J, Chandra K, Bansal S. Investigation of structural, magnetic, electrical and optical properties of chromium substituted cobalt ferrites ($CoCr_xFe_{2-x}O_4$, $0 \leq \times \leq 1$) synthesized using sol gel auto combustion method. J Mol Struct 2012;1012:182–8, http://dx.doi.org/10.1016/j.molstruc.2011.12.035.

[3] Rao TD, Karthik T, Asthana S. Investigation of structural, magnetic and optical properties of rare earth substituted bismuth ferrite. J Rare Earths 2013;31:370–5, http://dx.doi.org/10.1016/S1002-0721(12)60288-9.

[4] Gupta N, Dimri MC, Kashyap SC, Dube DC. Processing and properties of cobalt-substituted lithium ferrite in the GHz frequency range. Ceram Int 2005;31:171–6, http://dx.doi.org/10.1016/j.ceramint.2004.04.004.

[5] Schloemann E. Advances in ferrite microwave materials and devices. J Magn Magn Mater 2000;209:15–20, http://dx.doi.org/10.1016/S0304-8853(99)00635-6.

[6] Thomas N, Shimna T, Jithin PV, Sudheesh VD, Choudhary HK, Sahoo B, et al. Comparative study of the structural and magnetic properties of alpha and beta phases of lithium ferrite nanoparticles synthesized by solution combustion method. J Magn Magn Mater 2018;462:136–43, http://dx.doi.org/10.1016/j.jmmm.2018.05.010.

[7] Dasari M, Gajula G, Hanumantha R, Chintabathini A, Kurimella S, Somayajula B. Lithium ferrite: the study on magnetic and complex permittivity characteristics. Process

Appl Ceram 2017;11:7–12,
http://dx.doi.org/10.2298/PAC1701007D.

[8] Nicolas J, Wolfarth EP. Ferromagnetic Materials. Holland North Publ 1980.

[9] Raman R, Murthy VRK, Viswanathan B. Microwave dielectric loss studies on lithium-zinc ferrites. J Appl Phys 1991;69:4053–5, http://dx.doi.org/10.1063/1.348415.

[10] El-Shaarawy MG, Rashad MM, Shash NM, Maklad MH. Afifi FA. Structural, AC conductivity, dielectric behavior and magnetic properties of Mg-substituted $LiFe_5O_8$ powders synthesized by sol–gel auto-combustion method. J Mater Sci Mater Electron 2015;26:6040–50, http://dx.doi.org/10.1007/s10854-015-3181-2.

[11] Dipti Kumar P, Juneja JK, Singh S, Raina KK, Prakash C. Improved dielectric and magnetic properties in modified lithium-ferrites. Ceram Int 2015;41:3293–7, http://dx.doi.org/10.1016/j.ceramint.2014.10.092.

[12] Srivastava M, Layek S, Singh J, Das AK, Verma HC, Ojha AK, et al. Synthesis, magnetic and Mössbauer spectroscopic studies of Cr doped lithium ferrite nanoparticles. J Alloys Compd 2014;591:174–80, http://dx.doi.org/10.1016/j.jallcom.2013.12.180.

[13] Mazen SA, Abu-Elsaad NI. Structural, magnetic and electrical properties of the lithium ferrite obtained by ball milling and heat treatment. Appl Nanosci 2015;5:105–14.

[14] Zeng H, Tao T, Wu Y, Qi W, Kuang C, Zhou S, et al. Lithium ferrite ($Li_{0.5}Fe_{2.5}O4$) nanoparticles as anodes for lithium ion batteries. RSC Adv 2014;4:23145–8, http://dx.doi.org/10.1039/c4ra02957g.

[15] Surzhikov AP, Lysenko EN, Malyshev AV, Nikolaev EV, Zhuravkov SP, Vlasov VA. Investigation of the composition and electromagnetic properties of lithium ferrite $LiFe_5O_8$ ceramics synthesized from ultradisperse iron oxide. Russ Phys J 2015;57:1342–7, http://dx.doi.org/10.1007/s11182-015-0387-y.

[16] Rezlescu N, Doroftei C, Rezlescu E, Popa PD. Lithium ferrite for gas sensing applications. Sensors Actuators B Chem 2008;133:420–5, http://dx.doi.org/10.1016/j.snb.2008.02.047.

[17] Thakur P, Sharma P, Mattei JL, Queffelec P, Trukhanov AV, Trukhanov SV, et al. Influence of cobalt substitution on structural, optical, electrical and magnetic properties of nanosized lithium ferrite. J Mater Sci Mater Electron 2018;29:16507–15, http://dx.doi.org/10.1007/s10854-018-9744-2.

[18] Pachauri N, Khodadadi B, Althammer M, Singh AV, Loukya B, Datta R, et al. Study of structural and ferromagnetic resonance properties of spinel lithium ferrite ($LiFe_5O_8$) single crystals. J Appl Phys 2015;117:233907, http://dx.doi.org/10.1063/1.4922778.

[19] Vijaya Bhasker Reddy P, Ramesh B, Gopal Reddy C. Electrical conductivity and dielectric properties of zinc substituted lithium ferrites prepared by sol-gel method. Phys B Condens Matter 2010;405:1852–6, http://dx.doi.org/10.1016/j.physb.2010.01.062.

[20] Li B, Xie Y, Su H, Qian Y, Liu X. Synthesis of the nanocrystalline α-$LiFe_5O_8$ in a solvothermal process. Solid State Ion 1999;120:251–4, http://dx.doi.org/10.1016/S0167-2738(98)00556-6.

[21] Dar MA, Shah J, Siddiqui WA, Kotnala RK. Influence of synthesis approach on structural and magnetic properties of lithium ferrite nanoparticles. J Alloys Compd 2012;523:36–42, http://dx.doi.org/10.1016/j.jallcom.2012.01.083.

[22] Ernst FO, Kammler HK, Roessler A, Pratsinis SE, Stark WJ, Ufheil J, et al. Electrochemically active flame-made nanosized spinels: $LiMn_2O_4$, $Li_4Ti_5O_{12}$ and $LiFe_5O_8$. Mater Chem Phys 2007;101:372–8, http://dx.doi.org/10.1016/j.matchemphys.2006.06.014.

[23] Thakur A, Chevalier A, Mattei JL, Queffflec P. Low-loss spinel nanoferrite with matching permeability and permittivity in the ultrahigh frequency range. J Appl Phys 2010;108:1–5, http://dx.doi.org/10.1063/1.3455875.

[24] Fu YP, Lin CH. Microwave-induced combustion synthesis of powder and their characterization. J Appl Phys 2009;105:5–8, http://dx.doi.org/10.1063/1.3061931.

[25] Soibam I, Phanjoubam S, Prakash C. Mossbauer and magnetic studies of cobalt substituted lithium zinc ferrites prepared by citrate precursor method. J Alloys Compd 2009;475:328–31, http://dx.doi.org/10.1016/j.jallcom.2008.07.011.

[26] Dar MA, Batoo KM, Verma V, Siddiqui WA, Kotnala RK. Synthesis and characterization of nano-sized pure and Al-doped lithium ferrite having high value of dielectric constant. J Alloys Compd 2010;493:553–60, http://dx.doi.org/10.1016/j.jallcom.2009.12.154.

[27] Sattar AA, Agami WR. Study of the physical and magnetic properties of $Li_{0.3}Zn_{0.4-x}Ca_xFe_{2.3}O_4$ ferrite. J Alloys Compd 2010;496:341–4, http://dx.doi.org/10.1016/j.jallcom.2010.02.008.

[28] Rathod V, Anupama AV, VijayaKumar R, Jali VM, Sahoo B. Correlated vibrations of the tetrahedral and octahedral complexes and splitting of the absorption bands in FTIR spectra of Li-Zn ferrite. Vib Spectrosc 2017;92:267–72, http://dx.doi.org/10.1016/j.vibspec.2017.08.008.

[29] Al-Hilli MF, Li S, Kassim KS. Structural analysis, magnetic and electrical properties of samarium substituted lithiumnickel mixed ferrites. J Magn Magn Mater 2012;324:873–9, http://dx.doi.org/10.1016/j.jmmm.2011.10.005.

[30] Watawe SC, Bamne UA, Gonbare SP, Tangsali RB. Preparation and dielectric properties of cadmium substituted lithium ferrite using microwave-induced combustion. Mater Chem Phys 2007;103:323–8, http://dx.doi.org/10.1016/j.matchemphys.2007.02.037.

[31] Iqbal MJ, Haider MI. Impact of transition metal doping on Mössbauer, electrical and dielectric parameters of structurally modified lithium ferrite nanomaterials. Mater Chem Phys 2013;140:42–8, http://dx.doi.org/10.1016/j.matchemphys.2013.02.028.

[32] Gurav SK, Shirsath SE, Kadam RH, Mane DR. Low temperature synthesis of $Li_{0.5}Zr_xCo_xFe_{2.5-2x}O_4$ powder and their characterizations. Powder Technol 2013;235:485–92, http://dx.doi.org/10.1016/j.powtec.2012.11.009.

[33] Argentina GM, Baba PD. Microwave Lithium ferrites: an overview. IEEE Trans Microw Theory Tech 1974;22:652–8, http://dx.doi.org/10.1109/TMTT.1974.1128308.

[34] Ravinder D, Reddy PVB. Thermoelectric power studies of polycrystalline magnesium substituted lithium ferrites. J Magn Magn Mater 2003;263:127–33, http://dx.doi.org/10.1016/S0304-8853(02)01545-7.

[35] Prabhu YT, Rao KV. X-ray analysis by Williamson-Hall and size-strain plot methods of ZnO nanoparticles with fuel variation. WJNSE 2014:21–8, http://dx.doi.org/10.4236/wjnse.2014.41004.

[36] Mazen SA, Abu-Elsaad NI. Characterization and magnetic investigations of germanium-doped lithium ferrite. Ceram Int 2014;40:11229–37, http://dx.doi.org/10.1016/j.ceramint.2014.03.167.

[37] Caltun OF, Spinu L. Structure and magnetic properties of Ni-Zn-Cu ferrites sintered at different temperatures. J Optoelectron Adv M 2002;4:337–40.

[38] Manjurul Haque M, Huq M, Hakim MA. Influence of CuO and sintering temperature on the microstructure and magnetic properties of Mg-Cu-Zn ferrites. J Magn Magn Mater 2008;320:2792–9, http://dx.doi.org/10.1016/j.jmmm.2008.06.017.

[39] Iqbal MA, Islam MU, Ali I, Azhar M, Sadiq I, Ali I. High frequency dielectric properties of Eu^{+3}-substituted Li–Mg ferrites synthesized by sol–gel auto-combustion method. J Alloys Compd 2014;586:404–10, http://dx.doi.org/10.1016/j.jallcom.2013.10.066.

[40] Surzhikov AP, Malyshev AV, Lysenko EN, Vlasov VA, Sokolovskiy AN. Structural, electromagnetic, and dielectric properties of lithium-zinc ferrite ceramics sintered by pulsed electron beam heating. Ceram Int 2017;43:9778–82, http://dx.doi.org/10.1016/j.ceramint.2017.04.155.

[41] Nasir S, Saleemi AS, Fatima-tuz-Zahra, Anis-ur-Rehman M. Enhancement in dielectric and magnetic properties of Ni–Zn ferrites prepared by sol–gel method. J Alloys Compd 2013;572:170–4, http://dx.doi.org/10.1016/j.jallcom.2013.03.160.

[42] Collins T, Brown AE. LowLoss Lithium ferrites for microwave latching applications low-loss Lithium ferrites for microwave latching applications. J Appl Phys 1971;42, http://dx.doi.org/10.1063/1.1660752.

[43] Homes CC, Homes CC, Vogt T, Shapiro SM, Wakimoto S. Optical response of perovskite-related oxide. Science 2012;673, http://dx.doi.org/10.1126/science.1061655.

[44] Hiti ME. AC electrical conductivity of Ni-Mg ferrites. J Phys D Appl Phys 1996;29:501, http://dx.doi.org/10.1088/0022-3727/29/3/002.

[45] Kadam AA, Shinde SS, Yadav SP, Patil PS, Rajpure KY. Structural, morphological, electrical and magnetic properties of Dy doped Ni–Co substitutional spinel ferrite. J Magn Magn Mater 2013;329:59–64, http://dx.doi.org/10.1016/j.jmmm.2012.10.008.

[46] Cheruku R, Govindaraj G, Vijayan L. Super-linear frequency dependence of ac conductivity in nanocrystalline lithium ferrite. Mater Chem Phys 2014;146:389–98, http://dx.doi.org/10.1016/j.matchemphys.2014.03.043.

[47] Teixeira SS, Graca MPF, Costa LC, Valente MA. Study of the influence of thermal treatment on the magnetic properties of lithium ferrite prepared by wet ball-milling using nitrates as raw material. Mater Sci Eng 2014;186:83–8, http://dx.doi.org/10.1016/j.mseb.2014.03.008.

[48] Rathod V, Anupama AV, Jali VM, Hiremath VA, Sahoo B. Combustion synthesis, structure and magnetic properties of Li-Zn ferrite ceramic powders. Ceram Int 2017;43:14431–40, http://dx.doi.org/10.1016/j.ceramint.2017.07.213.

[49] Neel L. Magnetism and local molecular field. Science 1971;174:985–92, http://dx.doi.org/10.1126/science.174.4013.985 (80-).

[50] Hussein SI, Elkady AS, Rashad MM, Mostafa AG, Megahid RM. Structural and magnetic properties of magnesium ferrite nanoparticles prepared via EDTA-based sol-gel reaction. J Magn Magn Mater 2015;379:9–15, http://dx.doi.org/10.1016/j.jmmm.2014.11.079.

[51] Rashad MM, Nasr MI. Controlling the microstructure and magnetic properties of Mn-Zn ferrites nanopowders synthesized by co-precipitation method. Electron Mater Lett 2012;8:325–9, http://dx.doi.org/10.1007/s13391-012-1104-4.

[52] Melikhov Y, Snyder JE, Jiles DC, Ring AP, Paulsen JA, Lo CCH, et al. Temperature dependence of magnetic anisotropy in Mn-substituted cobalt ferrite. J Appl Phys 2006;99:08R102, http://dx.doi.org/10.1063/1.2151793.

[53] Shirsath SE, Kadam RH, Gaikwad AS, Ghasemi A, Morisako A. Effect of sintering temperature and the particle size on the structural and magnetic properties of nanocrystalline $Li_{0.5}Fe_{2.5}O_4$. J Magn Magn Mater 2011;323:3104–8, http://dx.doi.org/10.1016/j.jmmm.2011.06.065.

[54] Dar MA, Shah J, Siddiqui WA, Kotnala RK. Influence of synthesis approach on structural and magnetic properties of lithium ferrite nanoparticles. J Alloys Compd 2012;523:36–42, http://dx.doi.org/10.1016/j.jallcom.2012.01.083.

[55] Verma S, Joy PA. Low temperature synthesis of nanocrystalline lithium ferrite by a modified citrate gel precursor method. Mater Res Bull 2008;43:3447–56, http://dx.doi.org/10.1016/j.materresbull.2008.01.023.

[56] Verma V, Gairola SP, Pandey V, Tawale JS, Su H, Kotanala RK. High permeability and low power loss of Ti and Zn substitution lithium ferrite in high frequency range. J Magn Magn Mater 2009;321:3808–12, http://dx.doi.org/10.1016/j.jmmm.2009.07.044.

[57] Verma V, Sharma P, Singh A. Effect of iron content on permeability and power loss characteristics of $Li_{0.35}Cd_{0.3}Fe_{2.35}O_4$ and $Li_{0.35}Zn_{0.3}Fe_{2.35}O_4$. Bull Mater Sci 2014;37:855–9, http://dx.doi.org/10.1007/s12034-014-0017-2.